Universiteit Antwerpen

This item is the archived peer-reviewed author-version of:

Enhanced electrochemical performance of Li-rich cathode materials through microstructural control

Enhanced electrochemical performance of Li-rich cathode materials through microstructural control

Jon Serrano-Sevillano[†], Marine Reynaud[†], Amaia Saracibar[‡], Thomas Altantzis[§], Sara Bals[§], Gustaaf van Tendeloo[§], Montserrat Casas-Cabanas[†*]

† CIC energiGUNE, Parque Tecnológico de Álava, C/Albert Einstein 48, 01510 Miñano, Vitoria-Gasteiz, Álava, Spain

‡ Physical Chemistry Department, Basque Country University, Pharmacy Faculty, Vitoria-Gasteiz, Spain

§ Electron Microscopy for Materials Research (EMAT), University of Antwerp, 2020 Antwerp Belgium

ABSTRACT: The microstructural complexity of Li-rich cathode materials has so far hampered understanding the critical link between size, morphology, structural defects with both capacity and voltage fading that this family of materials exhibit. Li_2MnO_3 is used here as a model material to extract reliable structure-property relationships that can be further exploited for the development of high-performing and long-lasting Li-rich oxides. A series of samples with microstructural variability have been prepared and thoroughly characterized using the FAULTS software, which allows quantification of planar defects and extraction of average crystallite sizes. Together with transmission electron microscopy (TEM) and density functional theory (DFT) results, the successful application of FAULTS analysis to Li_2MnO_3 has allowed rationalizing the synthesis conditions and identifying the individual impact of concurrent microstructural features on both voltage and capacity fading. This clearly is a necessary step for the development of high-capacity Li-ion cathode materials with enhanced cycle life.

Li- and Mn-rich transition metal (TM) oxides ($x$$Li_2MnO_3$·(1-$x$)Li$MO_2$ or $Li_{1+x}M_{1-x}O_2$, where M = TM, typically Mn, Ni, Co) have attracted wide attention because they offer higher energy density, and are cheaper and environmentally more friendly than $LiCoO_2$. Indeed, these compounds are known to deliver >250 mAh/g of capacity at high voltage (2.5-4.8 V *vs.* Li$^+$/Li) as they combine cationic and anionic redox activity making them highly competitive to any commercial Li-ion cathode material.[1,2] However, despite these advantages, their cycle life is still severely limited by both capacity and voltage fading stemming from structural changes upon cycling.

Understanding such degradation mechanisms is hampered by the fact that neither their initial structure nor their microstructure is fully understood. This prevents elucidation of their chemical and structural reorganization during cycling and in particular on the first cycle.[3–6] In LiMO$_2$ layered structures, lithium layers and TM layers are alternately stacked following an O3 stacking sequence (ABCABC) according to Delmas' notation.[7] In Li_2MnO_3 (or Li[Li$_{1/3}$Mn$_{2/3}$]O$_2$, whose monoclinic structure (space group: *C2/m*) is shown in Figure 1 (a)), oxygen atoms are also arranged following an O3 stacking but excess lithium occupies TM sites, resulting in mixed Li and TM layers. Due to the different size of Li^I and Mn^{IV}, these atoms tend to arrange in a honeycomb configuration, in which the lithium atoms are surrounded by 6 TM atoms as illustrated in Figure 1 (b). Evidence of the superstructure resulting from the cationic ordering can be detected using different characterization techniques such as X-ray (XRD), Neutron (NPD) or electron (ED) diffraction as well as through transmission electron microscopy imaging.[8–10]

The exact structure of $Li_{1+x}M_{1-x}O_2$ (i.e. when Mn is partially replaced by Co or Ni) is however still under debate. While some groups claim that these compounds crystallize in the form of an intergrowth between Li_2MnO_3 and LiMO$_2$ nanodomains expressed as $x$$Li_2MnO_3$·(1-$x$)Li$MO_2$,[11,12] others defend a structure crystallizing as a solid solution which can be written as a single phase with formula $Li_{1+x}M_{1-x}O_2$.[13–17] In addition, as is often the case for layered materials, Li-rich layered oxides invariably exhibit large amounts of stacking faults rendering their structural and microstructural characterization extremely challenging.

A broad variety of structural arrangements can arise from disruptions in the stacking order of the Li_2MnO_3 layered structure. Two examples are shown in Figure 1 (c,d): one related to the oxygen stacking (c) and another to cationic ordering (d). The first one is the consequence of displacing a [Li$_{1/3}$Mn$_{2/3}$]O$_2$ layer 1/6 along both *a* and *b* axes in a *C2/m* unit cell. These can be for example represented as ABCABABC stacking sequence for an O1-type defect in the O3 structure.[7] The second type of defects results from a 1/3 displacement along both *a* and *b* axes in the *C2/m* unit cell, which causes a misalignment of the cationic ordering. Some authors use a number after the stacking letter to represent both kind of defects (i.e. A1B1C1A1B2C1; see Figure 1 (c,d)).[18,19] Note that the two types of defects are independent and could occur simultaneously. However, even if both cationic and oxygen stacking

1

defects are present there is no simple orientation where both can be observed simultaneously in TEM (note that there is a 30° rotation between the views of Figure 1 (c) and (d)). For simplicity and since O1-type defects are not significant in our samples (< 1% as shown below from our refinements of XRD data, and in accordance with the literature),[8] the stacking notation R (rectangular) and P and P' (parallelogram) proposed by Abraham's group,[20,21] is used here to describe the structural defects observed by TEM. The rectangular stacking refers to manganese dumbbells stacked on top of each other (ideal structure), whereas the parallelogram terms indicate layer displacements, as shown in Figure 1 (e).

Stacking faults, such as those in Figure 1 (d), result in a typical anisotropic broadening of some specific Bragg reflections in the XRD patterns: in particular, the $(020)_{C2/m}$ reflection exhibits a strong asymmetric broadening and the superstructure reflections appearing in the $20° \leq 2\theta_{Cu} \leq 35°$ range are strongly broadened. This results in the characteristic Warren fall these materials exhibit.[22] Conventional refinement models of XRD patterns, such as Le Bail or Rietveld methods, require the description of the crystal as a periodic unit cell extended along all directions in space, and thus do not allow taking into account non-periodic defects. An alternative approach, in which defective structures are described as a stack of atomic layers, first used in DIFFaX[23] for the simulation of diffraction patterns and later in the FAULTS software for the refinement of experimental data,[24–26] enables the quantification of planar defects from peak broadening and independently from finite size effects (see references 23-25 for more details). Shunmugasundaram et al.[18] used this program to study the effect of nickel in the stacking disorder of $Li[Li_{1/3-2x/3}Ni_xMn_{2/3-x/3}]O_2$ compounds and demonstrated that there is an increment in the number of stacking faults when the Ni content is increased. In a different study, Matsunaga et al.[27] showed that Li-rich compounds mostly exhibit stacking faults related to the honeycomb cationic ordering, with less than 1% of the defects related to the oxygen sublattice. However, neither the correlations between synthesis parameters and amount of defects, nor the individual impact of stacking faults on the capacity and cycling performance have been studied in detail for this system. Stacking faults have been suggested to beneficially contribute to capacity[28] although they have not been decoupled from size and morphology to date.

Proper understanding of the underlying thermodynamics, kinetics and degradation mechanisms of battery materials unavoidably requires a fundamental understanding of both structure and microstructure. In this work a series of microstructurally different Li_2MnO_3 samples have been prepared and thoroughly characterized. The combination of FAULTS refinements with TEM and DFT calculations applied to our model system Li_2MnO_3 has allowed rationalizing the synthesis conditions and identifying the individual impact of concurrent microstructural features on both voltage and capacity fading.
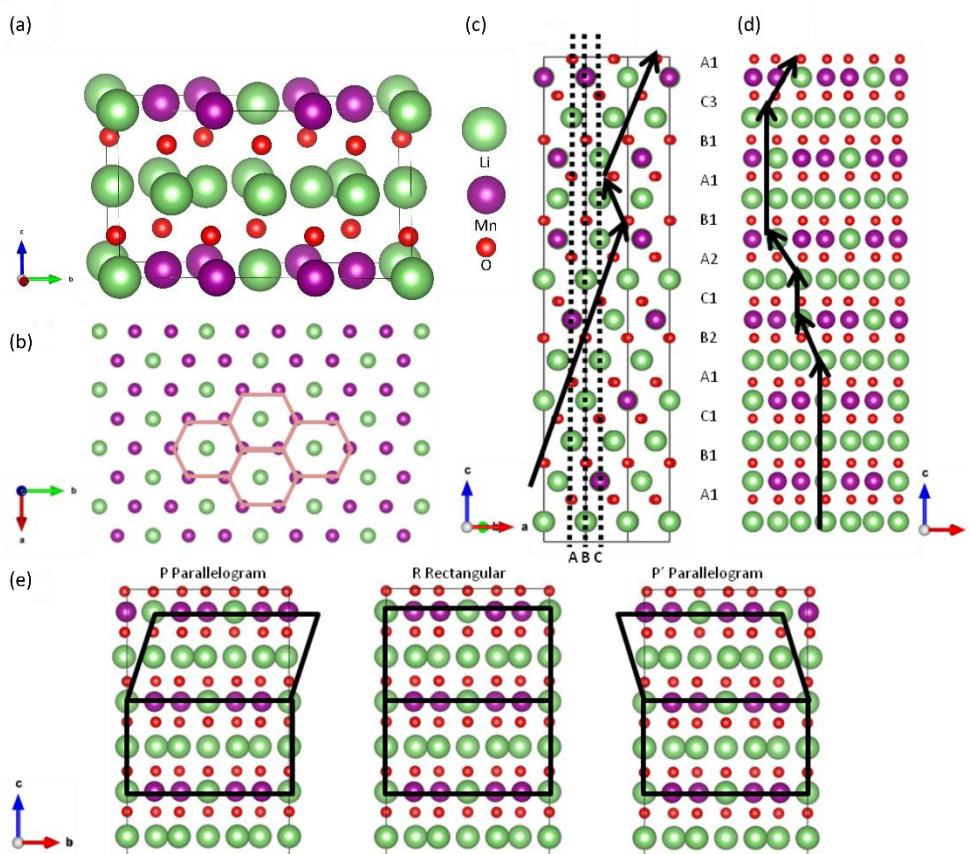

Figure 1. a) Ideal monoclinic structure of Li_2MnO_3 (space group: $C2/m$), where the different lithium positions are shown with different green colours; (b) *ab* plane of TM layers. The honeycomb arrangement is marked by the hexagons; (c) Visualization of stacking defects

related with the oxygen stacking; (d) Visualization of stacking defects related with cationic order; (e) Structural deviations arising from stacking faults related with cationic order using the notation of Abraham's group.[21]

Experimental section

Material synthesis. Mixtures of Li_2CO_3 and the Mn precursor (MnO, Mn_2O_3 or $MnCO_3$ were ball-milled for 5 minutes (SPEX SamplerPrep 8000 M Mixer/Mill) in a Li:Mn ratio 2.04:1 to compensate the Li loss occurring during the heat treatment. The mixture was then pelletized and submitted to a two-step heat treatment in air; the first one for 5 hours at 500°C and the second one at a selected temperature (700-900°C) for 5 hours unless otherwise specified. The obtained samples are labelled LMO_(precursor)_(temperature); for example, Li_2MnO_3 prepared from $MnCO_3$ at 900°C is here labeled as LMO_MnCO3_900.

X-ray Diffraction. XRD patterns were recorded on a Bruker D8 Discover instrument using a monochromatic copper radiation (Cu $K\alpha_1$ λ = 1.54053 Å). Patterns were measured in a 2θ range of 15-110° with a step size of 0.01° and a step time of 1.550 s. X-ray patterns were refined using both the FullProf[29,30] and the FAULTS[24,25] programs. Representations and analyses of the crystal structures were done using the program VESTA.[31–33]

Scanning Electron Microscopy. A small amount of powder was diluted in ethanol, sonicated for two minutes, deposited on a carbon film and analysed in a FEI Quanta 200 field-emission gun SEM.

Transmission Electron Microscopy. The samples were crushed in a mortar in acetone and the suspension was sonicated for a couple of minutes. Drops of this suspension were then deposited onto carbon-coated cupper grids. Selected Area Electron Diffraction (SAED) patterns and Energy Dispersive X-ray spectra (EDS) were acquired using a FEI Tecnai Osiris electron microscope, equipped with a ChemiSTEM system, and a FEI Tecnai G2 electron microscope, both operated at 200 kV. High-resolution High-Angle Annular Dark-Field Scanning Transmission Electron Microscopy (HAADF-STEM) images were acquired using an aberration corrected cubed FEI Titan electron microscope operated at 120 and 300 kV. Simulations of the ED patterns used for the indexation of the experimental SAED patterns were performed with the programs SingleCrystal (Demo version. Crystal Maker) and CaRIne Crystallography (version 3.1). FAULTS was also used to simulate the ED patterns of Li_2MnO_3 phases containing different amounts of stacking faults.

Electrochemical measurements. All the electrochemical measurements were carried out in half-cell configuration using CR2032-type coin cells assembled in an argon-filled glove-box. Positive electrodes were prepared by mixing Li_2MnO_3 samples with Kejten Black carbon and polyvinylidene fluoride (PVdF) binder (80:10:10 weight ratio), mixed for 5 minutes with IKA T25 digital ULTRA-TURRAX. A glassfiber separator was soaked with the electrolyte: a solution of 1.2 M $LiPF_6$ in ethylene carbonate (EC) and ethyl methyl carbonate (EMC) (3:7 in volume) with 5 wt% of 1-fluoroethylene carbonate (FEC) and 0.5 wt% of lithium bis(ethanedioato)borate (LiBOB) as additives. Lithium foil was used as reference and counter electrode. All the electrochemical tests were carried out at room temperature.

Computational details. The total energy of different Li_2MnO_3 stacking sequences was calculated using the Vienna Ab-initio Simulation Package (VASP).[34,35] Spin-polarized DFT calculations were performed. Projector augmented wave potentials[35] were used to replace core electrons whereas Li (2s), Mn (3p, 3d, 4s) and O (2s, 2p) valence electrons were expanded in plane-waves with a cut off energy of 600 eV. The Perdew-Burke-Ernzerhof (PBE)[36] exchange-correlation function was used together with a Monkhorst-Pack grid with 4 x 4 x 1 k-point sampling in 1 x 1 x 6 supercells. Initial defect-free and defect-containing supercells were built from the P1 model used with the FAULTS program, as explained in supplementary information. Structures were fully relaxed (cell parameters, volume cells and atomic positions) with a residual force threshold of 0.02 eV Å^{-1}. The generalized gradient approximation with the Hubbard parameter correction (GGA+U) of Dudarev et al.[37] was employed (with a U of 5 eV for Mn).[38] A convergence of the total energy close to 0.5 meV/fu (fu=formula unit) was achieved with these parameters.

Results and discussion

Synthesis and structural characterization. Since Li_2MnO_3 cannot be synthesized totally free of stacking faults even using high-temperature and/or long annealing times,[9,20] we used three different Mn precursors (MnO, Mn_2O_3 and $MnCO_3$) and different temperatures (700, 800 and 900°C) to obtain a set of samples with different size, morphology and amount of defects. Since Matsunaga et al.[8] did not notice any difference by changing the lithium precursor, Li_2CO_3 was used. The annealing time for most of the samples was 5 h although, in the case of LMO_MnO_700, 20 h were needed in order to form the pure phase (Figure S1 shows that after 5-hours of annealing the reaction was incomplete).
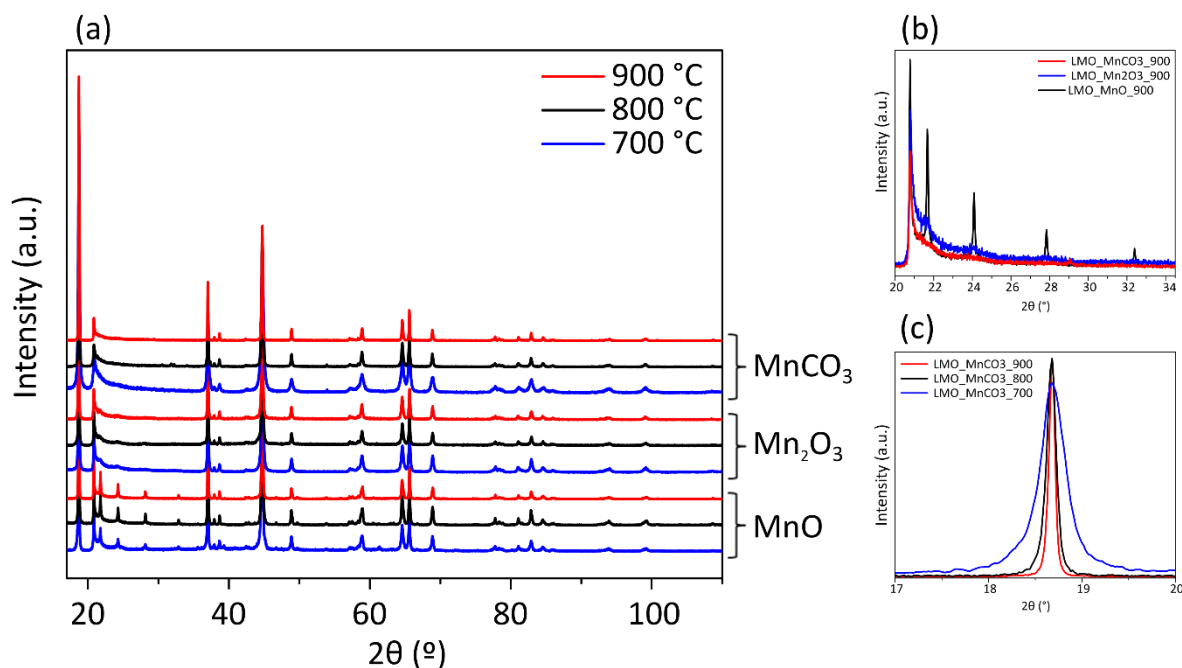
Figure 2. (a) Comparison of the XRD patterns of the different Li_2MnO_3 samples obtained from different precursors (MnO, Mn_2O_3 and $MnCO_3$) and annealing temperatures (700°C in blue, 800°C in black and 900°C in red); (b) Enlargement of the 2θ range 20°-35° for the samples synthesized at 900°C from different precursors where asymmetric peak broadening of the superstructure reflections arising from the presence of stacking faults (Warren fall) can be observed, and (c) enlargement of the 2θ range 17°-20° showing the peak broadening of the $(001)_{C2/m}$ reflection, which is not affected by stacking disorder, for samples prepared using $MnCO_3$ precursor at different temperatures.

In Figure 2, the XRD patterns of the samples prepared at 700°C, 800°C and 900°C are presented. Superstructure peaks can be clearly observed in the $20° \leq 2\theta \leq 35°$ range of all patterns when MnO is used as precursor. In turn, when Mn_2O_3 and $MnCO_3$ are used, superstructure peaks become weaker and broader and eventually collapse in a Warren-type fall.[22] Such diffuse intensity is also observed when MnO is used as precursor, especially at 700°C and 800°C but superstructure peaks are still visible, even for the lowest temperature used. As stacking faults are known to be at the origin of this asymmetric broadening, it can be (qualitatively) concluded that samples with the lowest amount of stacking faults are obtained when MnO is used as precursor. On the contrary, samples prepared using $MnCO_3$ as precursor exhibit the largest amount of stacking faults (Figure 2 (b)). To the best of our knowledge, the relevance of the choice of the Mn precursor has not been reported previously. Although most mixed Li-rich oxides are prepared by co-precipitation of mixed hydroxides for a homogeneous distribution of TMs, this is a relevant result for the design and understanding of high performance materials. On the other hand, particle size growth is also important as the synthesis temperature increases, especially for the samples synthesized from $MnCO_3$, as can be deduced from the broadening of the $(001)_{C2/m}$ reflection, which is not affected by stacking disorder (Figure 2 (c)).

Scanning Electron Microscopy (SEM). SEM was used to investigate the effect of the nature of the Mn precursor and of the annealing temperature on the particle size and shape. Figure 3 (a-c) shows SEM images of the samples synthesized from the $MnCO_3$ precursor at 700, 800 and 900°C respectively. In all cases quasi-spherical particles are observed, with increasing size as a function of temperature. When using Mn_2O_3 and MnO precursors (Figure 3 (d) and (e)), platelets are obtained, which are thinner for the Mn_2O_3 precursor. Therefore, the synthesis temperature has a major impact on the particle size, while the nature of the manganese precursor affects the particle shape. Figure S2 shows SEM images for all the synthesized samples.
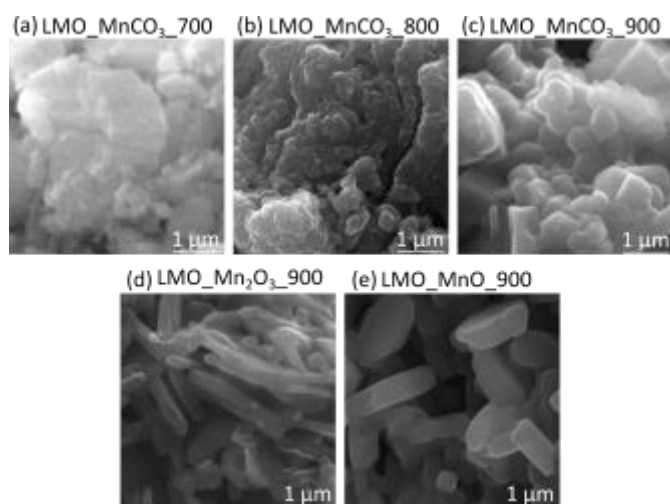

Figure 3. On top: SEM images showing the isotropic particles of the samples synthesized from $MnCO_3$ at (a) 700°C, (b) 800°C and (c) 900°C. On bottom: SEM images of the platelets constituting the samples synthesized at 900°C from (d) Mn_2O_3 and (e) MnO precursors.

4

Transmission Electron Microscopy (TEM) was employed to explore the statistical distribution of stacking faults within the particles. Samples LMO_MnO_900 and LMO_MnCO3_900 were chosen for presenting respectively the lowest and largest amounts of disorder according to the shape of the Warren fall observed in their XRD patterns (Figure 2). The O:Mn composition of both samples was investigated by EDS and confirmed their nominal composition.

All particles characterized by ED showed evidence of Li/Mn ordering in the TM slabs, through the presence of weak superstructure reflections and/or diffuse scattering lines between these superstructure reflections, parallel to the [001]* direction, i.e. the stacking direction of the TM slabs; in agreement with literature.[9,20,39] For both samples, SAED patterns were acquired along the [001] zone axis (Figure S3) and were indexed with the $C2/m$ monoclinic cell, which is typically used to describe Li_2MnO_3 (Figure 1 (a)). The SAED patterns presented in Figures 4 and S4 and which are acquired from crystals oriented along the [100] and/or <110> zone axes, present diffuse lines that evidence the existence of a considerable amount of stacking faults in the material along the c-axis (*i.e.* the direction of stacking of the TM layers). In the case of the LMO_MnO_900 sample, different kinds of SAED patterns have been observed: *(i)* some SAED patterns show sharp weak superstructure reflections, which can be unambiguously indexed either as the <110> one (Figure 4 (a)) or as the [100] zone axis (not shown) and correspond to the least defective zones; *(ii)* other SAED patterns corresponding to regions with an intermediate degree of defects (Figure 4 (b)) show both sharp weak reflections and more diffuse reflections, which can be indexed in the [100] and <110> respectively; *(iii)* finally other SAED patterns corresponding to highly defective regions (Figure 4 (c)) show continuous diffuse scattering lines instead of weak superstructure reflections, hampering a straightforward distinction between the [100] and the <110> zone axes. These three kinds of patterns can be observed within a single crystal by moving to different regions, indicating that the amount of stacking faults varies significantly within the same particle. For the LMO_MnCO3_900 sample the distribution of the defects is more homogeneous, since all the SAED patterns indexed along the [100]-<110> zone axes were similar and showed intense diffuse lines comparable to Figure 4 (c) (see Figure S4), evidencing a high amount of stacking

faults. Besides the presence of these diffuse lines, SAED patterns acquired along the [102] and [103] zone axes (Figure S3) also show additional weak reflections that are not consistent with the $C2/m$ monoclinic cell. However, these extra reflections can be explained as the intersection of diffuse scattering lines with Ewald's sphere (see Figure S5), as previously shown by Weill and co-workers.[39,40]

In order to get further insight in the distribution of stacking faults within the particles, we acquired HAADF-STEM images from different regions of samples LMO_MnO_900 and LMO_MnCO3_900. In Figure 5, HAADF-STEM images acquired from the edges and the bulk part of particles oriented along the [100]-<110> zone axes are presented. In this imaging mode, the intensity of the images is proportional to the atomic number Z^n ($1.6 < n < 2$),[41] meaning that the columns of heavier atoms will look brighter in the projection images compared to those of lighter elements. Therefore, the TM layers can be clearly observed. The Mn atomic columns are arranged in a dumbbell geometry along the direction perpendicular to the c-axis, and each Mn-Mn pair is separated by a column of Li atoms, which cannot be observed here due to its very low atomic number. Numerous changes in the stacking direction can be observed, which is in agreement with previous observations.[8,20,39] In Figure 5 (a) and (c), the changes in the stacking direction are highlighted using the R, P and P' notation (Figure 1 (e)). These images show that the stacking of TM slabs in Li_2MnO_3 samples resembles more a random stacking than a regular stacking containing some stacking errors. In addition, no regions with a regular alternation of stacking direction were observed at long range; a stacking of the type 1R-1P-1R-1P-1R would have been for example characteristic of the rhombohedral structure (space group: $P3_112$) proposed by Meng et *al*.[42,43] Besides these features, some isolated rows of Mn defects within some TM slabs could be observed (Figure 5 (b)). The sequence Mn dumbbell–blank–Mn dumbbell is lost, and replaced by a sequence of the type 1 Mn column–2 grey columns–1 Mn column. Such features have been also observed in previous reports.[8,44] They may be the result of either the loss of the honeycomb ordering within the TM layer (i.e. cation mixing), or twinning and antiphase defects within the TM layers with two different orientations of the honeycomb ordering in the same TM layer.
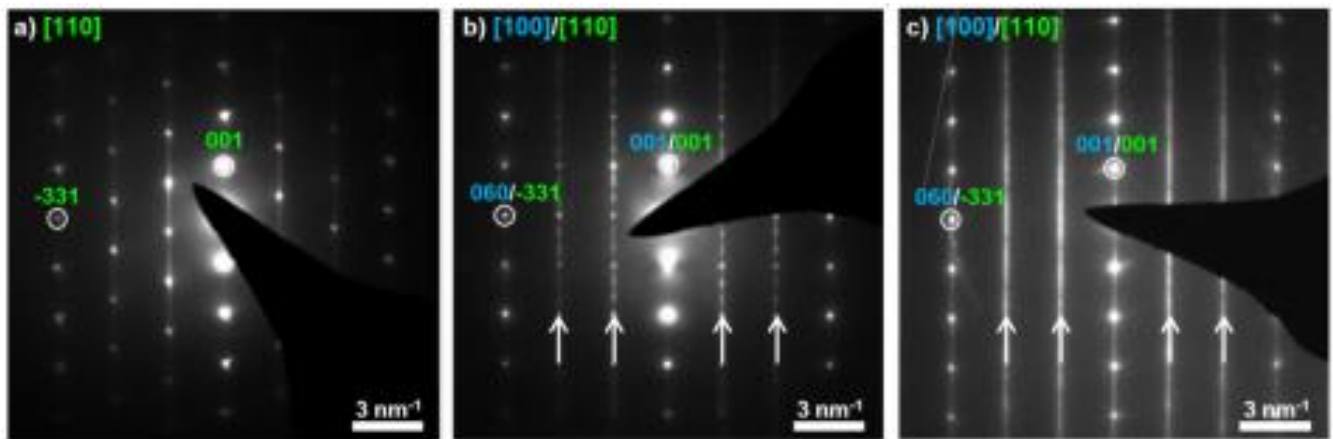

Figure 4. Representative SAED patterns from crystals of sample LMO_MnO_900, acquired along zone axes perpendicular to the direction of the stacking of the TM layers and indexed as $[100]_m$ or $<110>_m$.
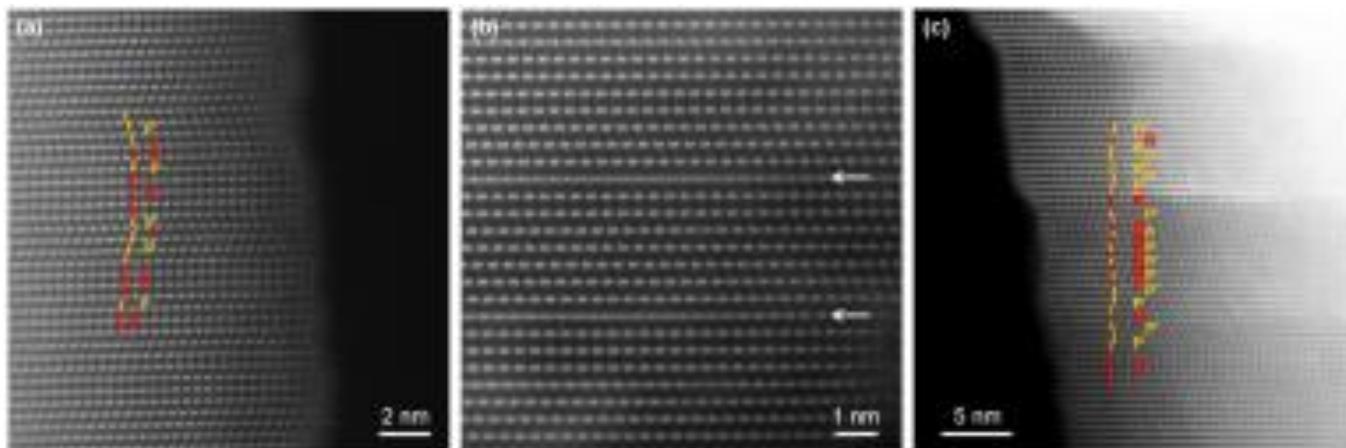
Figure 5. High-resolution HAADF-STEM images of different regions (a) from the edges and (b) from the bulk of a particle of sample LMO_MnO_900, oriented along the $[100]_m$-$<110>_m$ zone axis, and (c) from a particle of sample LMO_MnCO3_900 oriented along the $[100]_m$-$<110>_m$ zone axis. In (a) and (c) the red and yellow arrows indicate the R and P stackings, respectively, described in the main text and illustrated in Figure 1 (e). In (b) the white arrows indicate the defective rows of Mn atoms commented in the main text.

FAULTS refinements of XRD data. The presence of stacking faults in Li_2MnO_3 has generated some controversy for the determination of the space group to correctly describe its structure. Some authors used the $C2/c$ space group[45–47] or combined the $C2/m$ space group with a certain amount of $P3_112$ units.[42,43] The use of these two space groups was in fact an attempt to introduce stacking faults in the refinement of the structure. It is however now accepted that Li_2MnO_3 crystallizes in the $C2/m$ space group with different degrees of stacking faults. As refinement models such as the Rietveld method[48] typically do not allow stacking defects to be taken into account in the structure because these methods require a description of crystal structures using periodically repeated unit cells, in most refinements reported in the literature the range $20° \leq 2\theta_{Cu} \leq 35°$ is typically excluded or is improperly included in the background, with a consequent loss of important structural information. Here we have undertaken a more systematic analysis of the XRD patterns in order to extract quantitative information about both stacking defects and crystallite size thanks to the FAULTS program, which enables the full refinement of such defective structures.[24,26] The complete structural description used for these FAULTS refinements, in which the structure is described as a stack of atomic layers connected by stacking vectors associated to stacking probabilities, is detailed in supplementary information (section S3.1 and Figure S7). As mentioned before, three types of stacking are possible: the ideal stacking, R, and two types of stacking faults, P and P' (Figure 1 (e)). These stacking faults were treated as statistically equivalent, as previously done by Shunmugasundaram et al.[18] In addition, since high resolution HAADF-STEM had detected some Li/Mn mixing within the TM layers (Figure 5 (b)), this possibility was also taken into consideration in the refinements.

The following parameters were refined with FAULTS: scale factor, cell and profile parameters, stacking fault probabilities, atomic positions (except for lithium atoms) and Li/Mn exchange. Background was fitted with a linear interpolation of selected points and was manually refined. Thermal factors were fixed to 1. The XRD patterns of the samples synthesized from MnO were treated as two-phase mixtures to describe the particles as a combination of large defect-free and defective diffraction domains, in agreement with the high resolution HAADF-STEM observations. To do so, the ideal (defect-free) phase was simulated with the FullProf suite[29] and then included in the FAULTS refinement as a secondary phase, which was treated as background.[24] The scale of this secondary phase was refined in addition to the other parameters previously mentioned.
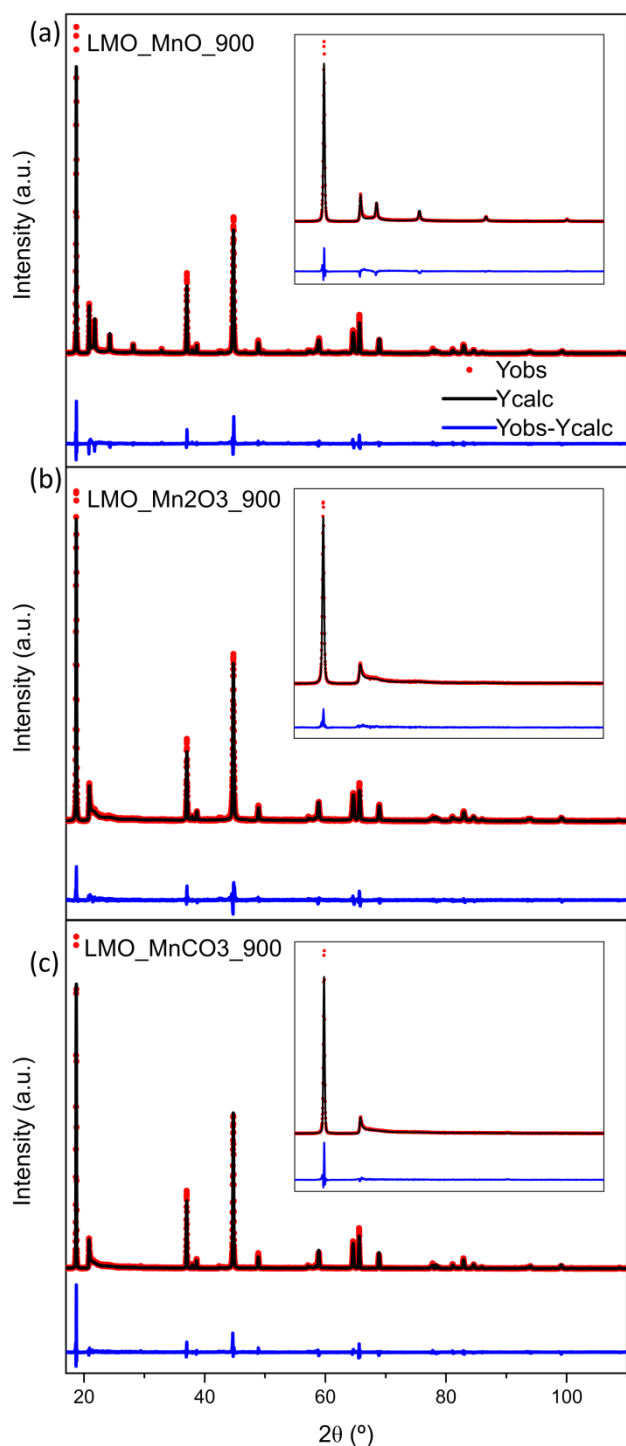
6

Figure 6. FAULTS refinement of the XRD patterns of the three samples (a) LMO_MnO_900, (b) LMO_Mn$_2$O$_3$_900 and (c) LMO_MnCO$_3$_900.

Figure 6 shows the refined patterns of (a) LMO_MnO_900, (b) LMO_Mn2O3_900 and (c) LMO_MnCO3_900; the refined parameters of all samples are shown in Table S2 and Table S3. For all the samples, the FAULTS refinements permitted to correctly fit the superstructure range $20° \leq 2\theta_{Cu} \leq 35°$ (set insets in Figure 6) and accurately refine the defective structures. FAULTS was also used to simulate

the ED patterns of the refined structures (see Figure S6), which confirm that the refined amount of stacking faults in these samples is large enough to make the superstructure reflection disappear in favor of diffuse scattering lines as observed the experimental SAED patterns (Figure 4 and Figure S4).

The average crystallite size was calculated for each sample from the refined profile parameters using Scherrer's formula[49] while their degree of defects was deduced from the refined stacking probabilities, as explained in supplementary information. The evolution of both the average crystallite size and the degree of defect are represented in Figure 7 (a, b) as a function of the synthesis temperature and the precursors used for each sample. As expected, and independently of the precursor used, the size of the crystallites increases with the annealing temperature. The sample synthesized from the MnCO$_3$ precursor at 700°C is the one exhibiting the smallest crystallite size; although the series of samples prepared from MnCO$_3$ also shows a more rapid growth when the annealing temperature increases. Interestingly, all samples exhibit a very similar crystallite size at 800°C, whereas at 900°C size broadening of the XRD peaks is only appreciated for the sample prepared from Mn$_2$O$_3$, with a resulting size of 250 nm. At 900°C, the size of the crystallites of the samples obtained from MnO and MnCO$_3$ is indeed too large (>500nm) to be precisely determined from diffraction data. Note that the average crystallite sizes calculated from FAULTS refinements are in good agreement with the particle sizes estimated from SEM images for all the samples.
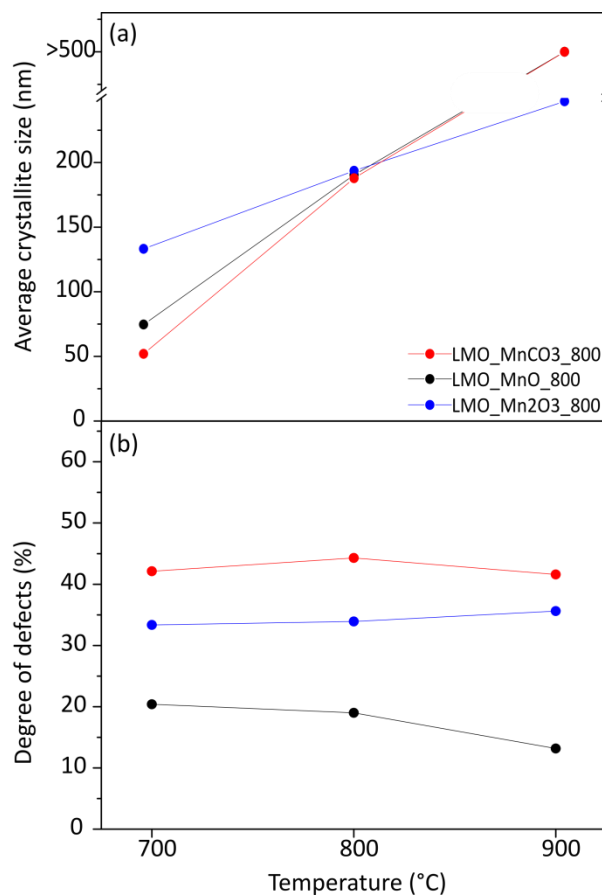

7

Figure 7. Temperature dependence of (a) the degree of defects and (b) the particle size of the samples synthesized from different precursors (in black MnO, in blue Mn_2O_3 and in red $MnCO_3$).

Regarding the degree of defects, the nature of the precursor has a stronger impact than the synthesis temperature, as shown in Figure 7 (b). Irrespective of the temperature used, $MnCO_3$ leads to the largest amount of defects (41 to 45%) while MnO produces the lowest amount (13 to 20%). Although the amount of defects is maintained with temperature when using $MnCO_3$ and Mn_2O_3 as precursors, the amount of defects in samples prepared from MnO slowly decreases with increasing the temperature.

In order to further understand the impact of reaction time and temperature on the microstructure of Li_2MnO_3, additional samples were prepared from $MnCO_3$: at 1000°C with the same reaction time as the previous samples (5 hours), and at 700°C, 900°C and 1000°C but with a longer reaction time (20h). The XRD patterns of these samples (Figure S8) show that an increase of the reaction time at 700°C and 900°C does not have a major impact on the reaction product. When increasing the temperature to 1000°C for 5 hours of annealing, superstructure peaks begin to appear from the Warren fall, and when annealing for longer time (1000°C for 20 h) further growth of the superstructure peaks is observed, although the Warren fall is maintained. Therefore longer annealing times are not sufficient to reduce the amount of defects when the temperature is not high enough. Once a threshold temperature is reached, annealing time will lead to the growth of defect-free domains.

The combination of electron microscopy and diffraction techniques allows one to conclude that the choice of the Mn precursor has a strong impact on the amount of stacking faults and the morphology of the particles; while temperature dominates the size of the crystallites (although the Mn precursor used also partially contributes). The precursors used in this work have indeed very different decomposition or melting temperatures and result in different decomposition products when calcined (Figure S9 and Figure S10). This results in different reaction paths and kinetics, leading to more or less rapidly grown crystals, with more disordered structures. Reaction time has an impact on the formation of the phase when the kinetics are slow (*e.g.* LMO_MnO_700 requires 20h of annealing), but it is not critical on defect growth at synthesis temperatures below 900°C.

DFT calculations. From a theoretical point of view, intensive work has been done aimed at understanding the structural stability of Li_2MnO_3 upon delithiation and its relationship with the electrochemical behavior. The thermodynamic of Li_2MnO_3 and the origin of the spinel phase transformation upon delithiation have been rationalized.[50–52] Li mobility,[50,53] the oxygen redox activity and its impact in the capacity of the material has been also investigated using First Principles calculations.[5,50,54–60] However, in all reported theoretical studies ideal and defect-free materials have been considered. In order to have a more complete overview of the system, we have carried out theoretical calculations to compare the relative stability of the structure containing several defective stackings.

We calculated the total energy of a series of hypothetical crystals of Li_2MnO_3 composition, built with a stack of 12 layers. In addition to the ideal structure (Figure 8 (a)), five other stacking sequences have been generated Figure 8 (b-g)) to evaluate the energy difference between the ideal and the defective structural arrangements. Figure 8 shows structures with one isolated defect (Figure 8 (b)), structures with two consecutive stacking faults (Figure 8 (c)) and structures with three (Figure 8 (d, e)) and five stacking defects (Figure 8 (f)). Additionally, an O1-type stacking fault was also considered (Figure 8 (g)). This unit cell is made of 8 layers instead of 12 so the O1 defect can be inserted in the middle of the O3 stacking sequence: AB**CACA**BC (8 layers for the O1 defect) instead of ABCABCABCABC (12 layers for the ideal stacking). As the total energy of the structure depends on the number of atoms, energy values have been normalized to the number of atoms contained in a $C2/m$ unit cell. The energy difference (ΔE) of each defective structure is shown with respect to that of the ideal structure. The results obtained indicate that all of them, with the exception of the O1-type defect, have a very similar energy. Although the ideal structure and the structures with a smaller number of defects (Figure 8 (a-d)) are slightly more stable than the structures with a larger number of defects per number of layers (Figure 8 (e-f)), no major differences between the different configurations are observed (the different sequences only differ by 0-40 meV). Our results show that the ideal structure is not the most energetically favorable, however this result must be taken with caution as the differences are very small and the DFT calculations do not include finite temperature. Thermodynamics indeed predict that structures containing small amounts of defects should be more favorable than the ideal ones.[61] It can therefore be concluded that at room temperature, the different stacking sequences are similarly favorable. This conclusion is in agreement with the fact that stacking faults cannot be totally suppressed under the conditions of temperature and time employed here.
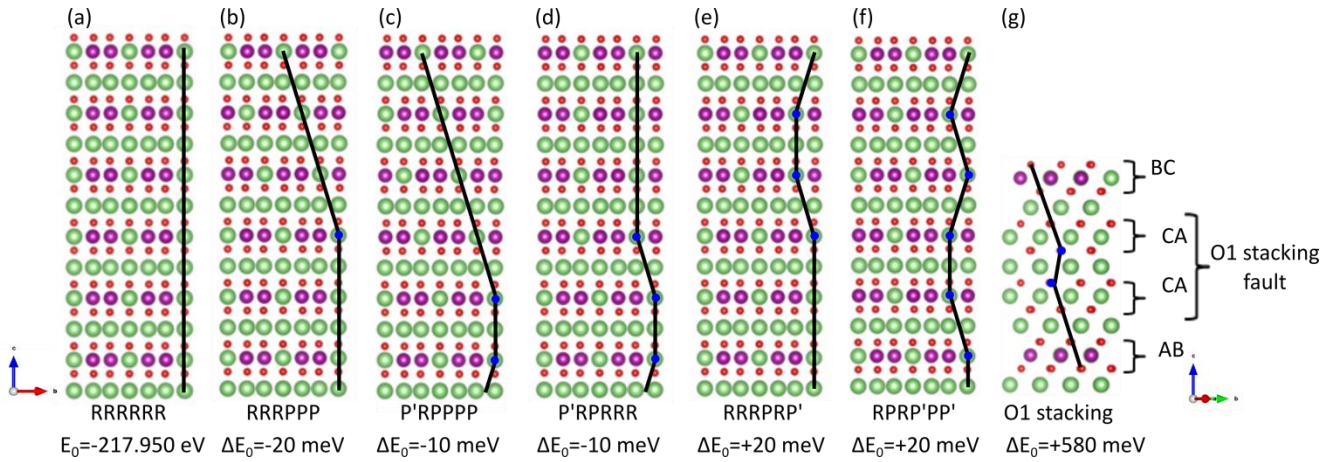
Figure 8. Structures analysed by DFT calculations with a different number of stacking faults. (a) Ideal stacking, (b-c) structure with one defect included, (d), (e) and (f) with 3, 3 and 5 defects included respectively and (g) the structure with an O1 type defect. Blue circles indicate the stacking faults.

Electrochemical characterization. Li_2MnO_3 was considered for many years as electrochemically inactive, since no additional Li could be introduced in its structure and Mn^{IV} cannot be further oxidized at these voltages. However, when charging small size grains above 4.5 V vs. Li^+/Li, a plateau is eventually observed, and the related structural transformations activate the material, which is then able to deliver a reversible capacity in the following cycles, as other Li-rich oxides.[62]

In order to better understand the impact of the microstructure on the electrochemical performances of Li_2MnO_3, galvanostatic experiments were performed on all the synthesized samples (Figure S11). A comparison of the capacity of the samples synthesized at 800°C, which exhibit similar particle size but differ in morphology and degree of defects, is shown in Figure 9 (a). LMO_MnCO3_800 shows by far the best performance while LMO_Mn2O3_800 and LMO_MnO_800 exhibit a much lower capacity. There is a clear correlation between the morphology of the particles and the capacity of the sample. The largest capacity is obtained with the sample with isotropic particles, having more available access points for the extraction/insertion of Li^+ ions than platelet-shaped particles, and thus allowing achieving a higher degree of activation. Interestingly, decoupling size and defects reveals that, contrary to previous reports in which this decoupling was not done,[8,63] the degree of defects does not show a clear correlation with the capacity. LMO_MnCO3_800 indeed exhibits the largest capacity and the highest amount of defects; however, if one compares LMO_Mn2O3_800 and LMO_MnO_800 samples which crystallize with similar shape and size but different degree of defects (black and blue curves in Figure 9 (a)), the defective platelet-shaped sample presents a lower capacity than the less-defective one.

Figure 9 (b) shows the effect of particle size on the capacity for samples prepared from $MnCO_3$. Particles with size of around 50 nm as determined from the FAULTS refinement achieve the maximum capacity in the first 10 cycles. However, after 20 cycles, the capacity starts fading and drastically drops. On the contrary, for the sample exhibiting the largest particle size (in red), the activation is extremely slow. The maximum capacity is achieved after 200 cycles and still does not reach the same as samples with lower particle size. When the parti-

cle size is around 200 nm, the compromise between fast activation and cycling stability is the best, reaching a stable capacity as high as that of the sample with the smallest particles around cycle 50. These three samples exhibit a very similar degree of defects and therefore these results again indicate that there is no correlation between stacking disorder and capacity.
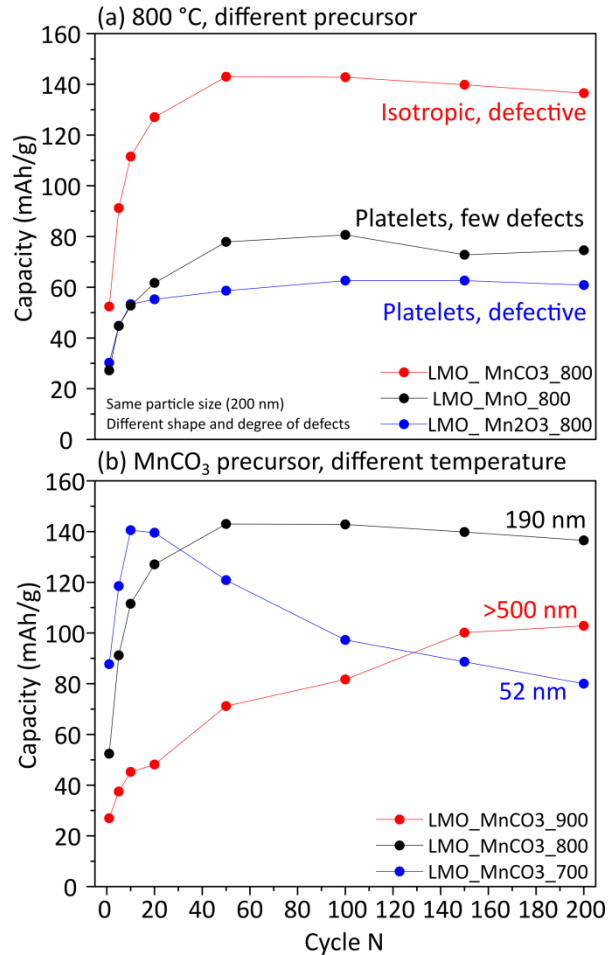
Figure 9. (a) Comparison of the capacity retention obtained for samples synthesized at 800 °C with same particle size. Samples synthesized from $MnCO_3$, Mn_2O_3 and MnO are represented by the red, blue and black lines respectively. (b) Comparison of the capacity retention obtained for samples synthesized from $MnCO_3$. Samples synthesized at 900°C, 800°C and 700°C are represented by the red, black and blue lines respectively. For both graphs, results for cycles 1, 5, 10, 20, 50, 100, 150 and 200 are included.

In order to understand the individual impact of microstructural features on the voltage fading, dQ/dV plots at cycles 10, 50 and 100 of the samples synthesized at 800°C (and therefore with the same particle size) are compared in Figure 10. Several peaks are observed: i) the activation peak at 4.7 V *vs.* Li^+/Li^0 (P1) that only appears at the early cycles and whose intensity decreases as the activation of the material is completed. This peak is attributed to structural rearrangement and O_2 release, both at the surface and in the bulk, as well as to electrolyte oxidation.[52,64,65] ii) a peak at around 4.3 V *vs.* Li^+/Li^0 in charge (P2) whose equivalent in discharge appears with a hysteresis of ~1 V (P7 at ~3.3 V *vs.* Li^+/Li^0). This peak is associated with oxygen redox activity and its hysteresis is thought to come from consecutive structural rearrangements whether caused by transition metal rearrangement due to lithium removal[51,66] or oxygen network distortion due to oxygen redox activity.[67–69] iii) a doublet of peaks at 4.0-4.2 V *vs.* Li^+/Li^0 in charge (P3) and 3.9-4.1 V *vs.* Li^+/Li^0 in discharge (P8). These peaks, not present in early cycles but visible in latter ones, are characteristic for $LiMn_2O_4$ spinel.[70] Some authors have previously evidenced lithium migration to tetrahedral positions from solid-state NMR and *in situ* XRD, which would be at the origin of the spinel phase formation.[71,72] iv) A peak at 3.8 V *vs.* Li^+/Li^0 in charge (P4) whose equivalent is found at ~3.1 V *vs.* Li^+/Li^0 in discharge, overlapping with P6 and P7. One can indeed see the apparition of a shoulder next to P6 between cycles 10 and 50, in particular in Figures 10 (b) and (c), which is probably the equivalent of the P4 peak in discharge. This peak is possibly related to manganese redox activity. v) A peak at 3.0 V *vs.* Li^+/Li^0 (P5) in charge and 2.9 V *vs.* Li^+/Li^0 (P6) in discharge. This peak is the signature of lithium insertion in octahedral positions.[66] Even if this peak is characteristic for spinel phase[70,73] it is already present at early stages, although the characteristic doublet for spinel at 4.0-4.2 V is not yet observed. Therefore, this peak could be the sum of two different peaks, one related with the aforementioned spinel material and the other with the activated MnO_2-like material.[64,74,75]

From the comparison of our set of samples, one can observe that the growth of the spinel doublet P3 is specially marked for the low-defect-containing sample (LMO_MnO_800), while it is retarded for the more defective samples (LMO_Mn2O3_800 and LMO_MnCO3_800). This is better appreciated in Figure S12 (a), where the contribution of this doublet of peaks to the total capacity is plotted as a function of the cycle number, evidencing that low-defect-containing particles lead to a higher amount of spinel since the first cycles (LMO_MnO_800). For the three samples, the contribution of spinel progressively increases at similar rate, and it remains thus significantly lower after 100 cycles in the more defective samples (LMO_Mn2O3_800 and LMO_MnCO3_800). On the other

hand, remarkable differences between the three samples are observed in the characteristic voltage fading occurring in Li_2MnO_3, which is primarily seen in the displacement of the discharge peak P7 at ~3.3 V *vs.* Li^+/Li^0 (while the corresponding charge peak P2 appears at a constant potential of 4.3 V *vs.* Li^+/Li^0). This voltage fading is indeed smaller for the sample with more defects and isotropic particles (LMO_MnCO3_800). This can also be better appreciated in Figure S12 (b) where the average voltage of peak P7 is compared around the cycles 10, 50 and 100 for the three samples synthesized at 800°C. Figure S13 shows similar trends for samples synthesized at 900°C for both the formation rate of spinel and the voltage fading, indicating that the particle size has no effect on those features and confirming the correlations previously described.

In view of these results, it can be concluded that the local environments created by stacking faults could stabilize manganese in the TM sites while being less favorable for migration of Mn to lithium slabs, thus delaying the formation of spinel environments. On the other hand, and independently of the obtained capacity, the voltage fading is not fully correlated with the increasing amount of spinel, since the evolution of spinel growth follows the same trend for the three samples (Figure S12 (a)) while the voltage fading evolves faster for platelet-shaped samples (Figure 10, Figure S12 (b) and Figure S13).

All in all, through microstructural control we have been able to obtain a sample (LMO_MnCO3_800) exhibiting isotropic shape and high degree of defects, which permit to reach high capacity as well as both low voltage and capacity fadings after 200 cycles. These observations represent a relevant step towards the mitigation of voltage and capacity fading in Li-rich layered oxides. Such approach could be extended to other battery materials undergoing microstructural transformations.
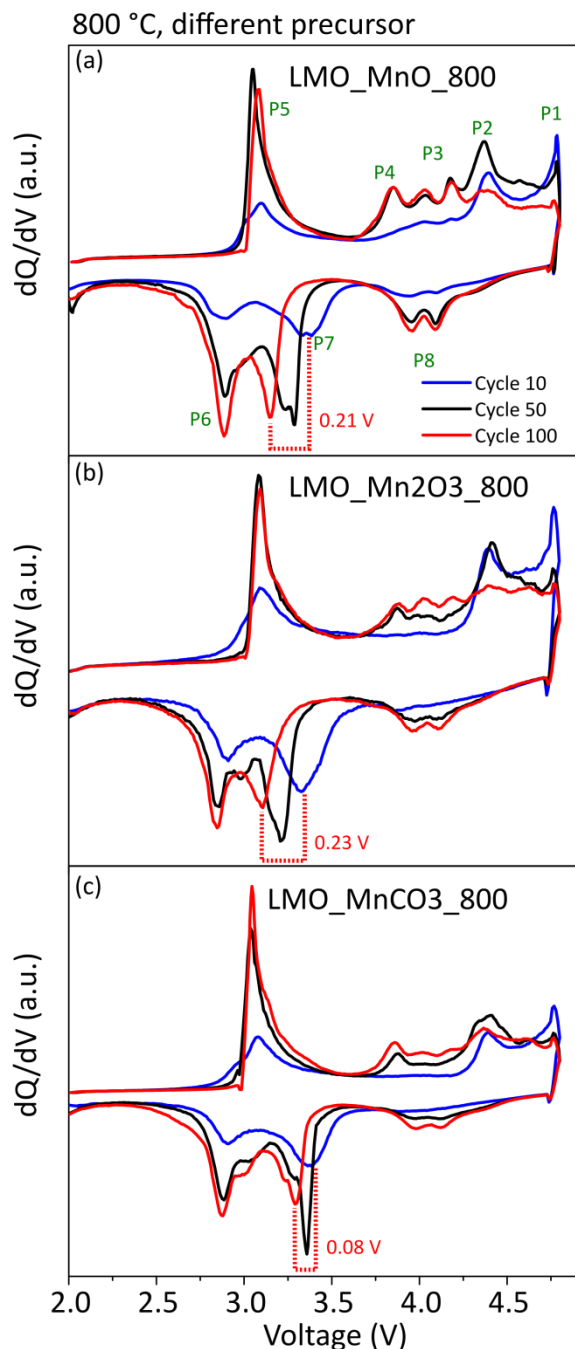
10

Figure 10. Derivative curves dQ/dV of the 10th, 50th and 100th galvanostatic cycles (blue, black and red lines, respectively) obtained for the samples synthesized at 800°C from (a) MnO, (b) Mn_2O_3 and (c) $MnCO_3$. The positions of the different oxidation and reduction peaks discussed in the text are indicated in green. The voltage difference of P7 between cycles 10 and 100 is highlighted with the red dashed line and the voltage difference is indicated.

CONCLUSIONS

A set of Li_2MnO_3 samples have been synthesized starting from different Mn precursors and using different temperatures. The samples obtained exhibit a large microstructural diversity (in terms of size, morphology and amount of defects) which has allowed rationalizing synthesis conditions and decoupling the individual role of each microstructural feature in the electrochemical properties. The use of FAULTS program has been key to extract quantitative correlations with crystallite size and amount of defects. It has been found that synthesis temperature has a strong impact on particle size, while the Mn precursor allows tuning the particles shape and the amount of defects. HAADF-STEM images, in agreement with DFT calculations, reveal that there are no preferential defective sequences and that stacking faults occur randomly. High capacities are achieved with the defective sample exhibiting spherical particles of around 200 nm, while low-defect samples convert faster to the spinel phase, seriously affecting cycling stability. Our results show that microstructural control is an extremely powerful tool as morphology, size and defects can be individually used for deterministically tuning and enhancing Li-rich electrochemistry. Understanding the role of defects in the spinel transformation mechanism could be crucial to improve the cell performance and opens a new strategy to be pursued in Li-rich materials.

ASSOCIATED CONTENT

Supporting Information.
Synthesis; Electron diffraction; FAULTS refinement of the XRD patterns; Stability tests.
This material is available free of charge via the Internet at http://pubs.acs.org.

AUTHOR INFORMATION

Corresponding Author

* Montse Casas-Cabanas. E-mail: mcasas@cicenergigune.com

Author Contributions

Conception and design of the work: MCC; DFT calculations: AS, JSS; Syntheses: JSS; XRD characterization: JSS, MCC; TEM: TA, MR, SB, GVT; Electrochemical characterization: JSS; Drafting and critical revision of the article: MCC, JSS, MR, AS, TA, SB, GVT. All authors have given their approval to the final version of the manuscript.

Notes

The authors declare no competing financial interest.

ACKNOWLEDGMENT

REFERENCES

(1) Xiang, Y.; Sun, Z.; Wu, X.; Liu, Z.; He, Z.; Long, B.; Yang, C.; Yin, Z. Improved Electrochemical Performance of Li1.2Ni0.2Mn0.6O2 Cathode Material for Lithium Ion Batteries Synthesized by the Polyvinyl Alcohol Assisted Sol-Gel Method. *Ceram. Int.* **2017**, *43* (2), 2320–2324.

(2) Liu, Y.; Wang, Q.; Zhang, Z.; Dou, A.; Pan, J.; Su, M. Investigation the Electrochemical Performance of Layered Cathode Material Li1.2Ni0.2Mn0.6O2 Coated with Li4Ti5O12. *Adv. Powder Technol.* **2016**, *27* (4), 1481–1487.

(3) Yan, P.; Xiao, L.; Zheng, J.; Zhou, Y.; He, Y.; Zu, X.; Mao, S. X.; Xiao, J.; Gao, F.; Zhang, J. G.; Wang, C. M. Probing the Degradation Mechanism of Li2MnO3 Cathode for Li-Ion Batteries. *Chem. Mater.* **2015**, *27* (3), 975–982.

(4) Rinaldo, S. G.; Gallagher, K. G.; Long, B. R.; Croy, J. R.; Bettge, M.; Abraham, D. P.; Bareño, J.; Dees, D. W. Physical Theory of Voltage Fade in Lithium- and Manganese-Rich Transition Metal Oxides. *J. Electrochem. Soc.* **2015**, *162* (6), A897–A904.

(5) Saubanère, M.; McCalla, E.; Tarascon, J.-M.; Doublet, M.-L. The Intriguing Question of Anionic Redox in High-Energy Density Cathodes for Li-Ion Batteries. *Energy Environ. Sci.* **2016**, *9* (3), 984–991.

(6) McCalla, E.; Abakumov, A. M.; Saubanere, M.; Foix, D.; Berg, E. J.; Rousse, G.; Doublet, M.-L.; Gonbeau, D.; Novak, P.; Van Tendeloo, G.; Dominko, R.; Tarascon, J.-M. Visualization of O-O Peroxo-like Dimers in High-Capacity Layered Oxides for Li-Ion Batteries. *Science (80-.).* **2015**, *350* (6267), 1516–1521.

(7) Delmas, C.; Fouassier, C.; Hagenmuller, P. Structural Classification and Properties of the Layered Oxides. *Phys. B+C* **1980**, *99* (1–4), 81–85.

(8) Matsunaga, T.; Komatsu, H.; Shimoda, K.; Minato, T.; Yonemura, M.; Kamiyama, T.; Kobayashi, S.; Kato, T.; Hirayama, T.; Ikuhara, Y.; Arai, H.; Ukyo, Y.; Uchimoto, Y.; Ogumi, Z. Dependence of Structural Defects in Li2MnO3 on Synthesis Temperature. *Chem. Mater.* **2016**, *28* (12), 4143–4150.

(9) Boulineau, A.; Croguennec, L.; Delmas, C.; Weill, F. Structure of Li2MnO3 with Different Degrees of Defects. *Solid State Ionics* **2010**, *180* (40), 1652–1659.

(10) Reynaud, M.; Casas-Cabanas, M. Order and Disorder in NMC Layered Materials: A FAULTS Simulation Analysis. *Powder Diffr.* **2017**, No. January, 1–8.

(11) Yu, H.; Ishikawa, R.; So, Y.-G.; Shibata, N.; Kudo, T.; Zhou, H.; Ikuhara, Y. Direct Atomic-Resolution Observation of Two Phases in the Li 1.2 Mn 0.567 Ni 0.166 Co 0.067 O 2 Cathode Material for Lithium-Ion Batteries. *Angew. Chemie Int. Ed.* **2013**, *52* (23), 5969–5973.

(12) Gu, M.; Belharouak, I.; Genc, A.; Wang, Z.; Wang, D.; Amine, K.; Gao, F.; Zhou, G.; Thevuthasan, S.; Baer, D. R.; Zhang, J. G.; Browning, N. D.; Liu, J.; Wang, C. Conflicting Roles of Nickel in Controlling Cathode Performance in Lithium Ion Batteries. *Nano Lett.* **2012**, *12* (10), 5186–5191.

(13) Koga, H.; Croguennec, L.; Mannessiez, P.; Ménétrier, M.; Weill, F.; Bourgeois, L.; Duttine, M.; Suard, E.; Delmas, C. Li1.20Mn0.54Co0.13Ni0.13O2 with Different Particle Sizes as Attractive Positive Electrode Materials for Lithium-Ion Batteries: Insights into Their Structure. *J. Phys. Chem. C* **2012**, *116* (25), 13497–13506.

(14) Lu, Z.; Chen, Z.; Dahn, J. R. Lack of Cation Clustering in Li[NixLi1/3-2x/3Mn2/3-x/3]O2 (0 < X E 1/2) and Li[CrxLi(1-x)/3Mn(2-2x)/3]O2 (0 < X < 1). *Chem. Mater.* **2003**, *15*, 3214–3220.

(15) Jarvis, K. A.; Deng, Z.; Manthiram, A.; Ferreira, P. J. Understanding the Role of Lithium Content on the Structure and Capacity of Lithium-Rich Layered Oxides by Aberration-Corrected STEM, D-STEM, and EDS. *Microsc. Microanal.* **2012**, *18* (S2), 1484–1485.

(16) Shukla, A. K.; Ramasse, Q. M.; Ophus, C.; Duncan, H.; Hage, F.; Chen, G. Unravelling Structural Ambiguities in Lithium- and Manganese-Rich Transition Metal Oxides. *Nat. Commun.* **2015**, *6* (May), 8711.

(17) Sathiya, M.; Ramesha, K.; Rousse, G.; Foix, D.; Gonbeau, D.; Prakash, A. S.; Doublet, M.-L.; Hemalatha, K.; Tarascon, J.-M. High Performance Li2Ru1−yMnyO3 (0.2 ≤ Y ≤ 0.8) Cathode Materials for Rechargeable Lithium-Ion Batteries: Their Understanding. *Chem. Mater.* **2013**, *25*, 1121–1131.

(18) Shunmugasundaram, R.; Arumugam, R. S.; Dahn, J. R. A Study of Stacking Faults and Superlattice Ordering in Some Li-Rich Layered Transition Metal Oxide Positive Electrode Materials. *J. Electrochem. Soc.* **2016**, *163* (7), A1394--A1400.

(19) Liu, J.; Yin, L.; Wu, L.; Bai, J.; Bak, S. M.; Yu, X.; Zhu, Y.; Yang, X. Q.; Khalifah, P. G. Quantification of Honeycomb Number-Type Stacking Faults: Application to Na3Ni2BiO6 Cathodes for Na-Ion Batteries. *Inorg. Chem.* **2016**, *55* (17), 8478–8492.

(20) Lei, C. H.; Wen, J. G.; Sardela, M.; Bareño, J.; Petrov, I.; Kang, S.-H.; Abraham, D. P. Structural Study of Li2MnO3 by Electron Microscopy. *J. Mater. Sci.* **2009**, *44* (20), 5579–5587.

(21) Bareño, J.; Lei, C. H.; Wen, J. G.; Kang, S. H.; Petrov, I.; Abraham, D. P. Local Structure of Layered Oxide Electrode Materials for Lithium-Ion Batteries. *Adv. Mater.* **2010**, *22* (10), 1122–1127.

(22) Biscoe, J.; Warren, B. E. An X-Ray Study of Carbon Black. *J. Appl. Phys.* **1942**, *13* (6), 364–371.

(23) Treacy, M. M. J.; Newsam, J. M.; Deem, M. W. A General Recursion Method for Calculating Diffracted Intensities from Crystals Containing Planar Faults. *Proc. R. Soc. A Math. Phys. Eng. Sci.* **1991**, *433* (1889), 499–520.

(24) Casas-Cabanas, M.; Reynaud, M.; Rikarte-Ormazabal, J.; Horbach, P.; Rodríguez-Carvajal, J. FAULTS: A Program for Refinement of Structures with Extended Defects. *J. Appl. Crystallogr.* **2016**, *49* (6), 2259–2269.

(25) Casas-Cabanas, M.; Rikarte-Ormazabal, J. FAULTS. Available as a Sub-Program of the FullProf Suite at Http://www.ill.eu/sites/fullprof, or as a Separate Program at Http://www.cicenergigune.com/faults. **2015**.

(26) Casas-Cabanas, M.; Rodríguez-Carvajal, J.; Palacín, M. R. FAULTS, a New Program for Refinement of Powder Diffraction Patterns from Layered Structures. In *Zeitschrift fur Kristallographie, Supplement*; 2006; Vol. 1, pp 243–248.

(27) Matsunaga, T.; Komatsu, H.; Shimoda, K.; Minato, T.; Yonemura, M.; Kamiyama, T.; Kobayashi, S.; Kato, T.; Hirayama, T.; Ikuhara, Y.; Arai, H.; Ukyo, Y.; Uchimoto, Y.; Ogumi, Z. Structural Understanding of Superior Battery Properties of Partially Ni-Doped Li2MnO3 as Cathode Material. *J. Phys. Chem. Lett.* **2016**, *7* (11), 2063–2067.

(28) Yu, D. Y. W.; Yanagida, K.; Kato, Y.; Nakamura, H. Electrochemical Activities in Li2MnO3. *J. Electrochem. Soc.* **2009**, *156* (6), A417--A424.

(29) Rodríguez-Carvajal, J. Recent Advances in Magnetic Structure Determination by Neutron Powder Diffraction. *Phys. B Condens. Matter* **1993**, *192*, 55–69.

(30) Rodríguez-Carvajal, J. Fullprof Suite. Available at Http://www.ill.eu/sites/fullprof/. **1993**.

(31) Momma, K.; Izumi, F. VESTA 3 for Three-Dimensional Visualization of Crystal, Volumetric and Morphology Data. *J. Appl. Crystallogr.* **2011**, *44* (6), 1272–1276.

(32) Momma, K.; Izumi, F. VESTA: A Three-Dimensional Visualization System for Electronic and Structural Analysis. *J. Appl. Crystallogr.* **2008**, *41* (3), 653–658.

(33) Momma, K.; Izumi, F. Vesta. Available at Http://jp-Minerals.org/vesta/en/.

(34) Kresse, G.; Furthmüller, J. Efficiency of Ab-Initio Total Energy Calculations for Metals and Semiconductors Using a Plane-Wave Basis Set. *Comput. Mater. Sci.* **1996**, *6* (1), 15–50.

(35) Kresse, G.; Joubert, D. From Ultrasoft Pseudopotentials to the Projector Augmented-Wave Method. *Phys. Rev. B* **1999**, *59* (3), 1758–1775.

(36) Perdew, J. P.; Burke, K.; Ernzerhof, M. Generalized Gradient Approximation Made Simple. *Phys. Rev. Lett.* **1996**, *77* (18), 3865–3868.

(37) Dudarev, S. L. L.; Botton, G. A.; Savrasov, S. Y.; Szotek, Z.; Temmerman, W. M.; Sutton, A. P. P. Electronic Structure and Elastic Properties of Strongly Correlated Metal Oxides from

First Principles:LSDA+U, SIC-LSDA and EELS Study of UO2 and NiO. *Electron. Struct. Elastic Prop.* **1998**, *166* (1), 429.

(38) Zhou, F.; Cococcioni, M.; Kang, K.; Ceder, G. The Li Intercalation Potential of LiMPO 4 and LiMSiO 4 Olivines with M = Fe, Mn, Co, Ni. *Electrochem. commun.* **2004**, *6* (11), 1144–1148.

(39) Boulineau, A.; Croguennec, L.; Delmas, C.; Weill, F. Reinvestigation of Li2MnO3 Structure: Electron Diffraction and High Resolution TEM. *Chem. Mater.* **2009**, *21* (18), 4216–4222.

(40) Weill, F.; Tran, N.; Croguennec, L.; Delmas, C. Cation Ordering in the Layered Li1+x(Ni0.425Mn0.425Co0.15)1 - xO2 Materials (X = 0 and 0.12). *J. Power Sources* **2007**, *172* (2), 893–900.

(41) Pennycook, S. J. Z-Contrast Stem for Materials Science. *Ultramicroscopy* **1989**, *30* (1–2), 58–69.

(42) Meng, Y. S.; Ceder, G.; Grey, C. P.; Yoon, W.-S.; Shao-Horn, Y. Understanding the Crystal Structure of Layered LiNi[sub 0.5]Mn[sub 0.5]O[sub 2] by Electron Diffraction and Powder Diffraction Simulation. *Electrochem. Solid-State Lett.* **2004**, *7* (6), A155.

(43) Meng, Y. S.; Ceder, G.; Grey, C. P.; Yoon, W.-S.; Jiang, M.; Bréger, J.; Shao-Horn, Y. Cation Ordering in Layered O3 Li[NixLi1/3-2x/3Mn2/3-x/3]O2 (0 < X < 1/2) Compounds. *Chem. Mater.* **2005**, *17* (9), 2386–2394.

(44) Phillips, P. J.; Bareño, J.; Li, Y.; Abraham, D. P.; Klie, R. F. On the Localized Nature of the Structural Transformations of Li2MnO3 Following Electrochemical Cycling. *Adv. Energy Mater.* **2015**, *5* (23), 1–12.

(45) Jansen, V. M.; Hoppe, R. Zur Kenntnis Der NaCI-Strukturfamilie: Neue Untersuchungen an Li2MnO3. *Z. anorg. allg. Chem* **1973**, *397*, 279–289.

(46) Riou, A.; Lecerf, A.; Gerault, Y.; Cudennec, Y. Etude Structurale de Li2MnO3. *Mater. Res. Bull.* **1992**, *27* (3), 269–275.

(47) Song, B.; Lai, M. O.; Lu, L. Influence of Ru Substitution on Li-Rich 0.55Li2MnO3·0.45LiNi1/3Co1/3Mn1/3O2 Cathode for Li-Ion Batteries. *Electrochim. Acta* **2012**, *80*, 187–195.

(48) Rietveld, H. M. A Profile Refinement Method for Nuclear and Magnetic Structures. *J. Appl. Crystallogr.* **1969**, *2* (2), 65–71.

(49) Patterson, A. L. The Scherrer Formula for X-Ray Particle Size Determination. *Phys. Rev.* **1939**, *56* (10), 978–982.

(50) Xiao, R.; Li, H.; Chen, L. Density Functional Investigation on Li 2 MnO 3. *Chem. Mater.* **2012**, *24* (21), 4242–4251.

(51) Lee, E.; Persson, K. A. Structural and Chemical Evolution of the Layered Li-Excess LixMnO3 as a Function of Li Content from First-Principles Calculations. *Adv. Energy Mater.* **2014**, *4* (15), 1400498.

(52) Lim, J.-M.; Kim, D.; Lim, Y.-G.; Park, M.-S.; Kim, Y.-J.; Cho, M.; Cho, K. The Origins and Mechanism of Phase Transformation in Bulk Li2MnO3: First-Principles Calculations and Experimental Studies. *J. Mater. Chem. A* **2015**, *3* (13), 7066–7076.

(53) Shin, Y.; Ding, H.; Persson, K. A. Revealing the Intrinsic Li Mobility in the Li2MnO3 Lithium-Excess Material. *Chem. Mater.* **2016**, *28* (7), 2081–2088.

(54) Ye, D.; Zeng, G.; Nogita, K.; Ozawa, K.; Hankel, M.; Searles, D. J.; Wang, L. Understanding the Origin of Li2MnO3 Activation in Li-Rich Cathode Materials for Lithium-Ion Batteries. *Adv. Funct. Mater.* **2015**, *25* (48), 7488–7496.

(55) Armstrong, A. R.; Holzapfel, M.; Novák, P.; Johnson, C. S.; Kang, S. H.; Thackeray, M. M.; Bruce, P. G. Demonstrating Oxygen Loss and Associated Structural Reorganization in the Lithium Battery Cathode Li[Ni0.2Li0.2Mn 0.6]O2. *J. Am. Chem. Soc.* **2006**, *128* (26), 8694–8698.

(56) Sathiya, M.; Rousse, G.; Ramesha, K.; Laisa, C. P.; Vezin, H.; Sougrati, M. T.; Doublet, M.-L.; Foix, D.; Gonbeau, D.; Walker, W.; Prakash, A. S.; Ben Hassine, M.; Dupont, L.; Tarascon, J.-M. Reversible Anionic Redox Chemistry in High-Capacity Layered-Oxide Electrodes. *Nat. Mater.* **2013**, *12* (9), 827–835.

(57) Armstrong, A. R.; Robertson, A. D.; Bruce, P. G. Overcharging Manganese Oxides: Extracting Lithium beyond Mn4+. *J. Power Sources* **2005**, *146* (1–2), 275–280.

(58) Luo, K.; Roberts, M. R.; Hao, R.; Guerrini, N.; Pickup, D. M.;

(58) Liu, Y.-S.; Edström, K.; Guo, J.; Chadwick, A. V.; Duda, L. C.; Bruce, P. G. Charge-Compensation in 3d-Transition-Metal-Oxide Intercalation Cathodes through the Generation of Localized Electron Holes on Oxygen. *Nat. Chem.* **2016**, *8* (7), 684–691.

(59) Delmas, C. Battery Materials: Operating through Oxygen. *Nat. Chem.* **2016**, *8* (7), 641–643.

(60) Seo, D.-H.; Lee, J.; Urban, A.; Malik, R.; Kang, S.; Ceder, G. The Structural and Chemical Origin of the Oxygen Redox Activity in Layered and Cation-Disordered Li-Excess Cathode Materials. *Nat. Chem.* **2016**, *8* (7), 692–697.

(61) West, A. R. Solid State Chemistry and Its Applications. *John Wiley Sons* **2007**.

(62) Kalyani, P.; Chitra, S.; Mohan, T.; Gopukumar, S. Lithium Metal Rechargeable Cells Using Li2MnO3 as the Positive Electrode. *J. Power Sources* **1999**, *80* (1–2), 103–106.

(63) Amalraj, S. F.; Sharon, D.; Talianker, M.; Julien, C. M.; Burlaka, L.; Lavi, R.; Zhecheva, E.; Markovsky, B.; Zinigrad, E.; Kovacheva, D.; Stoyanova, R.; Aurbach, D. Study of the Nanosized Li2MnO3: Electrochemical Behavior, Structure, Magnetic Properties, and Vibrational Modes. *Electrochim. Acta* **2013**, *97*, 259–270.

(64) Tan, X.; Liu, R.; Xie, C.; Shen, Q. Modified Structural Characteristics and Enhanced Electrochemical Properties of Oxygen-Deficient Li2MnO3-Δobtained from Pristine Li2MnO3. *J. Power Sources* **2018**, *374* (November 2017), 134–141.

(65) Francis Amalraj, S.; Markovsky, B.; Sharon, D.; Talianker, M.; Zinigrad, E.; Persky, R.; Haik, O.; Grinblat, J.; Lampert, J.; Schulz-Dobrick, M.; Garsuch, A.; Burlaka, L.; Aurbach, D. Study of the Electrochemical Behavior of the "inactive" Li 2MnO 3. *Electrochim. Acta* **2012**, *78*, 32–39.

(66) Croy, J. R.; Gallagher, K. G.; Balasubramanian, M.; Chen, Z.; Ren, Y.; Kim, D.; Kang, S.-H.; Dees, D. W.; Thackeray, M. M. Examining Hysteresis in Composite X Li 2 MnO 3 ·(1– X)LiMO 2 Cathode Structures. *J. Phys. Chem. C* **2013**, *117* (13), 6525–6536.

(67) Assat, G.; Foix, D.; Delacourt, C.; Iadecola, A.; Dedryvère, R.; Tarascon, J.-M. Fundamental Interplay between Anionic/cationic Redox Governing the Kinetics and Thermodynamics of Lithium-Rich Cathodes. *Nat. Commun.* **2017**, *8* (1), 2219.

(68) Assat, G.; Iadecola, A.; Delacourt, C.; Dedryvère, R.; Tarascon, J. M. Decoupling Cationic-Anionic Redox Processes in a Model Li-Rich Cathode via Operando X-Ray Absorption Spectroscopy. *Chem. Mater.* **2017**, *29* (22), 9714–9724.

(69) Assat, G.; Delacourt, C.; Corte, D. A. D.; Tarascon, J.-M. Practical Assessment of Anionic Redox in Li-Rich Layered Oxide Cathodes: A Mixed Blessing for High Energy Li-Ion Batteries. *J. Electrochem. Soc.* **2016**, *163* (14), A2965–A2976.

(70) Tarascon, J.-M. The Spinel Phase of LiMn2O4 as a Cathode in Secondary Lithium Cells. *J. Electrochem. Soc.* **1991**, *138* (10), 2859.

(71) Fell, C. R.; Qian, D.; Carroll, K. J.; Chi, M.; Jones, J. L.; Meng, Y. S. Correlation between Oxygen Vacancy, Microstrain, and Cation Distribution in Lithium-Excess Layered Oxides during the First Electrochemical Cycle. *Chem. Mater.* **2013**, *25* (9), 1621–1629.

(72) Dogan, F.; Long, B. R.; Croy, J. R.; Gallagher, K. G.; Iddir, H.; Russell, J. T.; Balasubramanian, M.; Key, B. Re-Entrant Lithium Local Environments and Defect Driven Electrochemistry of Li- and Mn-Rich Li-Ion Battery Cathodes. *J. Am. Chem. Soc.* **2015**, *137* (6), 2328–2335.

(73) Croy, J. R.; Kim, D.; Balasubramanian, M.; Gallagher, K.; Kang, S.-H.; Thackeray, M. M. Countering the Voltage Decay in High Capacity xLi2MnO3●(1–x)LiMO2 Electrodes (M=Mn, Ni, Co) for Li+-Ion Batteries. *J. Electrochem. Soc.* **2012**, *159* (6), A781.

(74) Reimers, J. N. Synthesis and Electrochemical Studies of LiMnO[sub 2] Prepared at Low Temperatures. *J. Electrochem. Soc.* **1993**, *140* (12), 3396.

(75) Sun, Y.; Cong, H.; Zan, L.; Zhang, Y. Oxygen Vacancies and Stacking Faults Introduced by Low-Temperature Reduction Improve the Electrochemical Properties of Li 2 MnO 3 Nanobelts

13

as Lithium-Ion Battery Cathodes. *ACS Appl. Mater. Interfaces* **2017**, *9* (44), 38545–38555.